

X-ray Evidence for a Buried Active Galactic Nucleus in UGC 5101

Masatoshi Imanishi ¹, Yuichi Terashima ², Naohisa Anabuki ², and Takao Nakagawa ²

ABSTRACT

We present X-ray observations of the ultraluminous infrared galaxy, UGC 5101, thought to contain a buried active galactic nucleus (AGN) based on observations in other wavebands. We detected an absorbed hard component at >3 keV, as well as soft emission in the energy range 0.5–2 keV. The soft X-ray component, possibly due to a modestly dust-obscured, extended starburst, has an absorption-corrected 0.5–2 keV X-ray luminosity of $L_X(0.5\text{--}2\text{ keV}) = 1.2 \times 10^{41}$ ergs s^{−1}. The 0.5–2 keV X-ray to infrared luminosity ratio is a factor of ~ 5 lower than typical values for a normal starburst, suggesting that this extended starburst is unlikely to be energetically dominant in UGC 5101. The most plausible origin of the absorbed hard component is the putative buried AGN. The 6.4 keV Fe K α emission line has a modest equivalent width (~ 400 eV), suggesting that this hard component is direct emission from the AGN, rather than a scattered component. The absorption-corrected 2–10 keV X-ray luminosity of the buried AGN was estimated to be $L_X(2\text{--}10\text{ keV}) \sim 5 \times 10^{42}$ ergs s^{−1}. The intrinsic 2–10 keV X-ray luminosity and the 2–10 keV X-ray to infrared luminosity ratio are both comparable to values measured for Mrk 463, a Seyfert-2 galaxy of similar infrared luminosity.

Subject headings: galaxies: nuclei — X-ray: galaxies – galaxies: individual (UGC 5101)

¹National Astronomical Observatory, 2-21-1, Osawa, Mitaka, Tokyo 181-8588, Japan; imanishi@optik.mtk.nao.ac.jp

²The Institute of Space and Astronautical Science, 3-1-1 Yoshinodai, Sagami-hara, Kanagawa 226-8510, Japan

1. Introduction

Ultraluminous infrared galaxies (ULIRGs) detected by the *IRAS* all-sky survey radiate large, quasar-like luminosities ($> \text{a few} \times 10^{45} \text{ ergs s}^{-1}$) as infrared dust emission (Sanders et al. 1988); therefore they must consist of extremely powerful energy sources that are obscured by dust. ULIRGs have also been found at large distances ($z > 0.3$), where they have been used to trace the dust-obscured star formation rate, dust content, and metallicity of the early universe (Blain et al. 1999). However, it remains unclear whether ULIRGs are powered by dust-obscured active galactic nuclei (AGNs) or starbursts.

It is now widely accepted that the energetically dominant components in the majority of ULIRGs are compact ($< \text{a few } 100 \text{ pc}$), highly dust-obscured nuclear energy sources, rather than extended ($\sim \text{kpc}$), weakly obscured starburst activity (Soifer et al. 2000). It is essential to determine whether these compact energy sources consist of AGNs and/or compact starbursts. Approximately 30% of ULIRGs classified optically as Seyferts are known to possess energetically important AGNs surrounded by dust with the geometry of a *torus* (Veilleux, Kim, & Sanders 1999a; Veilleux, Sanders, & Kim 1999b). However, the AGNs expected to reside in the majority of non-Seyfert ULIRGs may be deeply buried in dust along all lines of sight. It is necessary to determine the energetic importance of such *buried* AGNs in order to understand the true nature of ULIRGs.

To estimate the relative energetic contributions of an AGN and a starburst, it is necessary to utilize signatures that are produced by only one of these processes. One such signature is the polycyclic aromatic hydrocarbon (PAH) emission found in the infrared 3–15 μm wavelength range (Allamandola et al. 1989). PAH emission is usually observed in a normal starburst, but not detected in a pure AGN (Moorwood 1986; Roche et al. 1991). Thus, PAH emission can be used to detect starburst emission, by disentangling from AGN emission, in an AGN/starburst composite, such as a ULIRG, and PAH luminosity traces the starburst’s absolute magnitude (Mouri et al. 1990; Genzel & Cesarsky 2000; Imanishi 2002). The 3.3 μm PAH emission feature and dust absorption features found in infrared 3–4 μm spectra have been used to detect candidates for non-Seyfert ULIRGs possessing energetically important buried AGNs (Imanishi & Dudley 2000; Imanishi, Dudley, & Maloney 2001; Imanishi & Maloney 2003).

One example of this type of object is UGC 5101 ($z = 0.040$). It has an infrared (8–1000 μm) luminosity of $L_{\text{IR}} \sim 3 \times 10^{45} \text{ ergs s}^{-1}$, a cool far-infrared color (*IRAS* 25 μm -to-60 μm flux ratio of < 0.2), and is optically classified as a LINER, based on a systematic spectral classification of galaxies (Veilleux et al. 1995). Imanishi et al. (2001) found the observed infrared 3–4 μm spectrum of UGC 5101 to be best explained by the presence of a powerful buried AGN. Imanishi & Maloney (2003) argued that the nuclear energy source in UGC 5101

is more centrally concentrated than nuclear gas and dust, as is expected for a buried AGN, rather than a normal starburst, which shows a mixed dust geometry (Soifer et al. 2000). Radio VLBI observations (Smith et al. 1998; Lonsdale et al. 2003) and a near-infrared high spatial resolution image obtained with *HST* (Scoville et al. 2000) also detected compact, high surface-brightness emission, which was interpreted as an AGN by these authors. Therefore, there is mounting evidence for the presence of a buried AGN in this galaxy. The detection of strong, absorbed 2–10 keV X-ray emission can provide compelling evidence for a powerful buried AGN, because an AGN is a much stronger 2–10 keV X-ray emitter than a starburst. Previous X-ray observations with *Chandra* failed to find clear evidence for X-ray emission from the putative AGN (Ptak et al. 2003). Here, we report analysis of high quality X-ray data of UGC 5101 obtained with *XMM* and *Chandra*. The high spectral sensitivity of *XMM* at 2–10 keV was fully utilized to detect absorbed hard X-ray emission from the putative buried AGN. *Chandra* data are used to investigate the X-ray morphology, benefiting from its high image quality, as well as to check the overall spectral consistency with the *XMM* spectrum. Throughout this Letter, we use a cosmology of $H_0 = 75 \text{ km s}^{-1} \text{ Mpc}^{-1}$, $\Omega_M = 0.3$, and $\Omega_\Lambda = 0.7$.

2. Observations and Data Analysis

An *XMM* observation of UGC 5101 was performed with the EPIC cameras (PN, MOS1, and MOS2) in full-frame mode on 2001 November 12. We used standard data analysis procedures with the XMM Science Analysis Software (SAS version 5.4), together with standard software packages (FTOOLS 5.2 and XSPEC 11.2). Time intervals with high background count rates were removed from the events files, and we included only events corresponding to patterns 0–4 for PN and 0–12 for MOS, as suggested in the SAS Handbook. The resulting exposure times, after screening for time intervals with high background, were 25.1 and 33.1 ksec for PN and MOS, respectively. We used the most recent calibration files retrieved from the XMM web page and response matrices created with SAS for our data analysis.

We extracted a source spectrum using a 22.5 arcsec radius circular region. A background spectrum was extracted from a nearby source-free circular region with a radius of 60 arcsec. We binned the spectra so that each energy channel contained a minimum of 20 counts. An absorbed hard X-ray component was clearly detected only in the PN spectrum, which contains the most counts. Therefore, we used the PN spectrum to obtain rough measurements of important parameters. However, to improve the statistics, final spectral fitting was performed using the combined PN, MOS1 and MOS2 spectra. We allowed the relative normalizations of the cameras to vary in our spectral fits as there is some uncertainty in the

relative flux calibration of the three cameras.

A *Chandra* observation was performed on 2001 May 28 with the ACIS-S3 back-illuminated CCD chip. The data were reprocessed using CIAO 2.2.1 and CALDB 2.17. An effective exposure time of 47.8 ksec was obtained after discarding high background intervals.

A *Chandra* spectrum of the nucleus was extracted from a circular region with a radius of 8 arcsec. A background spectrum was extracted from an annular region around the nucleus and subtracted from the nuclear spectrum. The spectrum was binned to facilitate the detection of emission-line features. The *C*-statistic was used to fit the spectrum since the number of events in each bin is small.

3. Results

Figure 1 shows a 0.5–2 keV *Chandra* image. The source is extended beyond the PSF of *Chandra* (~ 1 arcsec diameter for $>85\%$ encircled energy).

Figure 2a shows the *XMM* EPIC spectrum of UGC 5101. In addition to the soft emission dominating the 0.5–2 keV X-ray range, an absorbed hard component at >3 keV and emission line at ~ 6.5 keV were clearly seen. The hard component is likely to originate in the putative buried AGN, and so we fitted this component with a power-law model. The emission line at ~ 6.5 keV is likely to be the neutral Fe K α line at 6.4 keV, and was fitted with a narrow Gaussian profile. For the soft component, a 0.5–1 keV thermal emission model (mekal model in XSPEC) from a starburst was first attempted to fit the soft X-ray spectrum, particularly the apparent spectral peak at 0.7–1 keV. However, significant residuals were present in this model fit. Therefore, we added (A) higher temperature thermal emission (5–10 keV) from hot gas and X-ray binaries in a starburst, or (B) a second power-law component, which could be due to Thomson scattering of the power-law emission from the AGN. Table 1 summarizes the best-fit parameters for these models. To estimate the power of the putative buried AGN, the most important measurement is the absorption-corrected 2–10 keV X-ray luminosity of the hard component, $L_X(2-10 \text{ keV})$. Both models result in a similar $L_X(2-10 \text{ keV})$ of $\sim 5 \times 10^{42} \text{ ergs s}^{-1}$ and have a 6.4 keV Fe K α line of modest equivalent width ($\text{EW}_{6.4} \sim 400 \text{ eV}$). We varied some of the model parameters within reasonable ranges (e.g., a power-law photon index of $\Gamma = 1.0-2.0$, a temperature between 5–9 keV for the high-temperature thermal emission, and abundances of 0.1–0.4 solar for the thermal emission); however, these changes result in values of $L_X(2-10 \text{ keV})$, which are consistent within a factor of <2 .

Figure 2b shows the *Chandra* ACIS spectrum. The solid line overplotted for comparison is based on model A (in Table 1) from the *XMM* EPIC spectrum, with normalization of the

continuum and of the Gaussian component representing the Fe K α line as free parameters and were determined from the *Chandra* ACIS spectrum. The overall spectral shape is very similar to the *XMM* spectrum. In the soft energy band, several emission lines are seen: strong He-like Si (~ 1.9 keV) and He-like S (~ 2.5 keV). We detected the absorbed hard component, but the amount of absorption of this component is not well constrained from the *Chandra* spectrum alone, because of the paucity of photons at the highest energies (> 7 keV).

The Fe K α emission feature at 6.4 keV is also detected in the *Chandra* spectrum. To estimate its equivalent width, we fitted the *Chandra* spectrum in the 4–7.5 keV band to minimize uncertainties in the modeling of the continuum. Model A (in Table 1) was applied to the continuum. The equivalent width was estimated to be $EW_{6.4} = 230^{+320}_{-230}$ eV ($\Delta\chi^2 = 2.7$). This value is similar to the estimate based on the *XMM* EPIC spectrum (Table 1). The extremely large equivalent width ($5.9^{+624}_{-3.2}$ keV, $\Delta\chi^2 = 4.605$) reported by Ptak et al. (2003) was not confirmed with our analysis.

4. Discussion

4.1. Energetic Importance of Extended Starburst Activity

UGC 5101 shows starburst activity with spatial extension of a few kpc (~ 4 arcsec) in the east-west direction (Genzel et al. 1998), with dust obscuration at a level similar to that of the nearby prototypical starburst galaxy M82 in both mixed-dust and foreground-screen dust models (McLeod et al. 1993; Sturm et al. 2000). The extended morphology seen in the *Chandra* 0.5–2 keV image (~ 4 arcsec in the east-west direction; Fig.1) and the detection of emission lines in our spectra (Fig.2) suggest that thermal emission from the extended starburst contributes significantly to the soft X-ray emission below 2 keV. Assuming that all of the soft X-ray emission is of thermal origin (model A in Table 1), the absorption-corrected 0.5–2 keV soft X-ray luminosity is $L_X(0.5\text{--}2 \text{ keV}) \sim 1.2 \times 10^{41} \text{ ergs s}^{-1}$, which results in $L_X(0.5\text{--}2 \text{ keV})/L_{\text{IR}} \sim 4 \times 10^{-5}$.

In a starburst galaxy, the 0.5–2 keV X-ray to far-infrared (40–500 μm) luminosity ratio is typically $L_X(0.5\text{--}2 \text{ keV})/L_{\text{FIR}} \sim 2 \times 10^{-4}$ (Ranalli, Comastri, & Setti 2003). As the far-infrared (40–500 μm) and infrared (8–1000 μm ; Sanders & Mirabel 1996) luminosities do not differ very much in an ordinary starburst, the $L_X(0.5\text{--}2 \text{ keV})/L_{\text{IR}}$ ratio in UGC 5101 is a factor of ~ 5 lower than the value expected for a normal starburst. If some fraction of the soft X-ray emission originates in scattering of the power-law AGN component, this discrepancy is even larger. In UGC 5101, the ratio of starburst-tracing 6.2 μm PAH luminosity (measured using large-aperture spectroscopy with *ISO*; Spoon et al. 2002) to infrared luminosity, is

also lower by a factor of ~ 4 than that of a normal starburst (Imanishi & Maloney 2003). As the properties of the extended starburst in UGC 5101 are not expected to differ significantly from a normal starburst, these results both suggest that the modestly obscured extended starburst is unlikely to be the dominant energy source in UGC 5101.

4.2. A Buried Energy Source

As the hard X-ray component is strongly absorbed, it cannot originate in X-ray binaries from the modestly obscured extended starburst (Persic & Raphaeli 2002). The most plausible origin is an AGN deeply buried in gas and dust at the core. The modest equivalent width of the 6.4 keV Fe $K\alpha$ line suggests that direct X-ray emission from the AGN is detected, because in physically plausible AGN geometries, a scattered X-ray component is expected to show a very large (>1 keV) equivalent width (Matt, Guainazzi, & Maiolino 2003). If the absorbed hard component is direct emission, we find an absorption-corrected 2–10 keV luminosity for the buried AGN of $L_X(2\text{--}10\text{ keV}) \sim 5 \times 10^{42} \text{ ergs s}^{-1}$ (§ 3). In principle, the modest $EW_{6.4}$ of the detected hard component could be produced in a scattering situation, *if* it is Thomson scattered by highly ionized gas. If this is the case, the intrinsic $L_X(2\text{--}10\text{ keV})$ is even higher than our estimate above.

The $L_X(2\text{--}10\text{ keV})/L_{\text{IR}}$ ratio for UGC 5101 is $\sim 2 \times 10^{-3}$. $L_X(2\text{--}10\text{ keV})$ values have been measured for some Seyfert-2 infrared luminous galaxies ($L_{\text{IR}} > \text{a few} \times 10^{45} \text{ ergs s}^{-1}$) where the detected 2–10 keV emission is interpreted as a direct component, because of the modest equivalent widths of the 6.4 keV Fe $K\alpha$ emission (<1 keV). Examples include IRAS 20460+1925 (Ogasaka et al. 1997), IRAS 23060+0505 (Brandt et al. 1997), PKS 1345+12 (Imanishi & Ueno 1999), and Mrk 463 (Ueno et al. 1996). All are thought to be powered by AGNs, with no detectable starburst activity in the infrared (Genzel et al. 1998; Veilleux, Sanders, & Kim 1999b; Imanishi & Dudley 2000; Imanishi 2002). The $L_X(2\text{--}10\text{ keV})/L_{\text{IR}}$ ratios of these known AGN-powered, Seyfert-2, infrared luminous galaxies are between 0.002 and 0.02, with Mrk 463 having the lowest value ($L_X(2\text{--}10\text{ keV}) \sim 4 \times 10^{42} \text{ ergs s}^{-1}$; Ueno et al. 1996, $L_{\text{IR}} \sim 2 \times 10^{45} \text{ ergs s}^{-1}$). A smaller value of $L_X(2\text{--}10\text{ keV})/L_{\text{IR}}$ is expected for a buried AGN than for a Seyfert-2 AGN surrounded with dust in a toroid geometry, because in the former case, a larger fraction of the photons emitted from the AGN are absorbed by dust and re-emitted in the infrared. Thus, the buried AGN in UGC 5101 is likely to be as powerful as that in Mrk 463, in terms of both absolute 2–10 keV X-ray luminosity and ratio to infrared luminosity.

Regardless of whether the primary energy source of UGC 5101 is a buried AGN or a starburst, the large infrared luminosity is produced by UV emission. The contribution from

the detected X-ray-emitting buried AGN to the total energy output in the infrared depends highly on the intrinsic UV to 2–10 keV X-ray luminosity ratio; this is poorly understood and could vary substantially among the population of AGNs. The buried AGN could account for the bulk of the infrared luminosity in UGC 5101 if its intrinsic UV to 2–10 keV ratio is similar to the AGN in Mrk 463.

By applying a template of infrared spectral energy distribution of a *classical*, moderately infrared luminous AGN and a *normal* starburst to UGC 5101, Farrah et al. (2003) argued that infrared dust emission flux from UGC 5101 at $\lambda < 10 \mu\text{m}$ is dominated by an AGN, while that at $\lambda = 10\text{--}1000 \mu\text{m}$ is dominated by a starburst. This conclusion comes primarily from the known fact that a classical AGN generally shows a warmer infrared color than a normal starburst (de Grijp, Miley, & Lub 1987). However, ULIRGs are known to have a larger column density of obscuring dust than classical, less infrared luminous AGNs (Spoon et al. 2002; Imanishi & Maloney 2003), and thus infrared emission from the buried AGNs in ULIRGs should be cooler than that from classical AGNs. Furthermore, a significant fraction of dust grains in UGC 5101 was found to be ice-covered (Spoon et al. 2002; Imanishi & Maloney 2003), which also causes the infrared color to be cooler than bare dust grains (Dudley, Imanishi, & Maloney 2003). Therefore, a much larger fraction of the infrared dust emission from UGC 5101 at $>10 \mu\text{m}$ can be produced by the buried AGN than that estimated by Farrah et al.. Indeed, if an observed excess in the $60 \mu\text{m}$ luminosity function at the highest luminosity end, over the extrapolation from lower luminosity, is caused by AGN contribution (Takeuchi et al. 2003), then it is suggested that AGN-powered dust emission can contribute significantly to the luminosities of ULIRGs at as long as $60 \mu\text{m}$. These factors should be taken into account to correctly understand the origin of strong dust emission from UGC 5101 at $\lambda > 10 \mu\text{m}$.

Y.T. and N.A. are supported by the Japan Society for the Promotion of Science. The anonymous referee gave useful comments.

REFERENCES

- Allamandola, L. J., Tielens, A. G. G. M., & Barker, J. R. 1989, ApJS, 71, 733
- Blain, A. W., Smail, I., Ivison, R. J., & Kneib, J. -P. 1999, MNRAS, 302, 632
- Brandt, W. N., Fabian, A. C., Takahashi, K., Fujimoto, R., Yamashita, A., Inoue, H., & Ogasaka, Y. 1997, MNRAS, 290, 617
- de Grijp, M. H. K., Miley, G. K., & Lub, J. 1987, A&AS, 70, 95

- Dudley, C. C., Imanishi, M., & Maloney, P. R. 2003, *Astrophysics of Dust*, Estes Park, Colorado, May 26 - 30, 2003. ed. A. N. Witt. (in press)
- Farrah, D., Afonso, J., Efstathiou, A. Rowan-Robinson, M., Fox, M., & Clements, D. 2003, *MNRAS*, 343, 585
- Genzel, R. et al. 1998, *ApJ*, 498, 579
- Genzel, R., & Cesarsky, C. J. 2000, *ARA&A*, 38, 761
- Imanishi, M. 2002, *ApJ*, 569, 44
- Imanishi, M., & Ueno, S. 1999, *ApJ*, 527, 709
- Imanishi, M., & Dudley, C. C. 2000, *ApJ*, 545, 701
- Imanishi, M., Dudley, C. C., & Maloney, P. R. 2001, *ApJ*, 558, L93
- Imanishi, M., & Maloney, P. R. 2003, *ApJ*, 588, 165
- Lonsdale, C. J., Lonsdale, C. J., Smith, H. E., & Diamond, P. J. 2003, *ApJ*, 592, 804
- Matt, G., Guainazzi, M., & Maiolino, R. 2003, *MNRAS*, 342, 422
- McLeod, K. K., Rieke, G. H., Rieke, M. J., & Kelly, D. M. 1993, *ApJ*, 412, 111
- Moorwood, A. F. M. 1986, *A&A*, 166, 4
- Mouri, H., Kawara, K., Taniguchi, Y., & Nishida, M. 1990, *ApJ*, 356, L39
- Ogasaka, Y., Inoue, H., Brandt, W. N., Fabian, A. C., Kii, T., Nakagawa, T., Fujimoto, R., & Otani, C. 1997, *PASJ*, 49, 179
- Persic, M., & Raphaeli, Y. 2002, *A&A*, 382, 843
- Ptak, A., Heckman, T., Strickland, D., Levenson, N. A., & Weaver, K. 2003, *ApJ*, 592, 782
- Ranalli, P., Comastri, A., & Setti, G. 2003, *A&A*, 399, 39
- Roche, P. F., Aitken, D. K., Smith, C. H., & Ward, M. J. 1991, *MNRAS*, 248, 606
- Sanders, D. B., Soifer, B. T., Elias, J. H., Madore, B. F., Matthews, K., Neugebauer, G., & Scoville, N. Z. 1988, *ApJ*, 325, 74
- Sanders, D. B., & Mirabel, I. F. 1996, *ARA&A*, 34, 749

- Scoville, N. Z. et al. 2000, *AJ*, 119, 991
- Smith, H. E., Lonsdale, C. J., & Lonsdale, C. J. 1998, *ApJ*, 492, 137
- Soifer, B. T. et al. 2000, *AJ*, 119, 509
- Spoon, H. W. W., Keane, J. V., Tielens, A. G. G. M., Lutz, D., Moorwood, A. F. M., & Laurent, O. 2002, *A&A*, 385, 1022
- Sturm, E., Lutz, D., Tran, D., Feuchtgruber, H., Genzel, R., Kunze, D., Moorwood, A. F. M., & Thornley, M. D. 2000, *A&A*, 358, 481
- Takeuchi, T. T., Yoshikawa, K., & Ishii, T. T. 2003, *ApJ*, 587, L89
- Ueno, S., Koyama, K., Awaki, H., Hayashi, I., & Blanco, P. R. 1996, *PASJ*, 48, 389
- Veilleux, S., Kim, D. -C., Sanders, D. B., Mazzarella, J. M., & Soifer, B. T. 1995, *ApJS*, 98, 171
- Veilleux, S., Kim, D. -C., & Sanders, D. B. 1999a, *ApJ*, 522, 113
- Veilleux, S., Sanders, D. B., & Kim, D. -C. 1999b, *ApJ*, 522, 139

Table 1. Fitting results of the XMM data of UGC 5101.

Model	$\chi^2/\text{d.o.f.}$	kT [keV]	N_{H} [10^{23} cm^{-2}]	$L_{\text{TH}}(0.5\text{--}2\text{keV})$ [$10^{40} \text{ ergs s}^{-1}$]	$L_{\text{PL}}(2\text{--}10\text{keV})$ [$10^{42} \text{ ergs s}^{-1}$]	EW [eV]
(1)	(2)	(3)	(4)	(5)	(6)	(7)
A	45.7/46	$0.7^{+0.2}_{-0.3}$	14^{+1}_{-2}	12	7	410^{+270}_{-240}
B	50.5/46	$0.6^{+0.3}_{-0.4}$	12^{+2}_{-1}	3	6	330^{+240}_{-200}

Note. — Col. (1): Adopted best-fit models. Model A is absorbed power law ($\Gamma = 1.8$ fixed) + 0.7 keV thermal + 10 keV (fixed) thermal + narrow Gaussian (6.4 keV Fe $K\alpha$). Model B is absorbed power law ($\Gamma = 1.8$ fixed) + 0.6 keV thermal + second power law ($\Gamma = 1.8$ fixed; scattered component) + narrow Gaussian. In both models, the Galactic absorption is included. For thermal components, a mekal model, a fixed abundance of 0.5 solar, and plasma density of 1 cm^{-3} were adopted. Col. (2): Reduced χ^2 value. Col. (3): Temperature for soft thermal emission. The uncertainty is for 90% confidence level for one parameter of interest ($\Delta\chi^2 = 2.7$) throughout this Table. Col. (4): Absorption for the main power law component. Col. (5): Absorption corrected 0.5–2 keV luminosity for thermal emission. In model A, both 0.7 keV and 10 keV thermal components were added. Col. (6): Absorption corrected 2–10 keV luminosity for the primary power law component. Col. (7): Equivalent width of the 6.4 keV Fe $K\alpha$ emission line, relative to the main power law component.

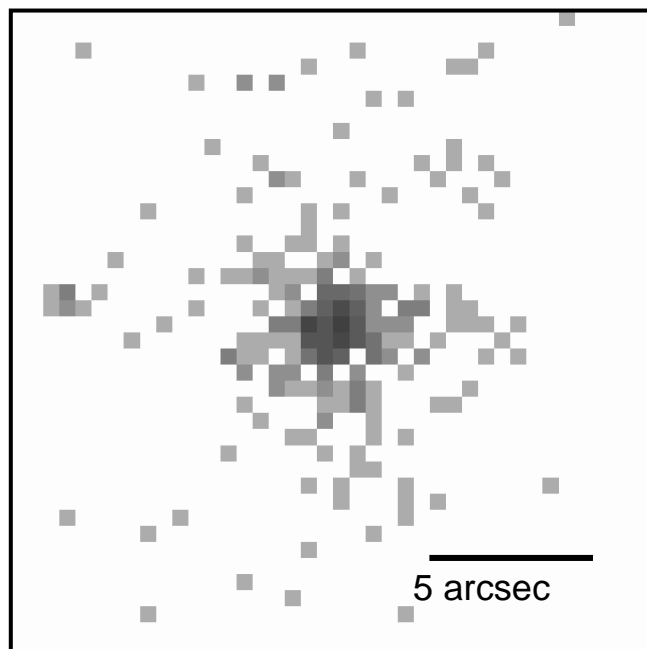


Fig. 1.— A *Chandra* image of UGC 5101 in the 0.5–2 keV X-ray band.

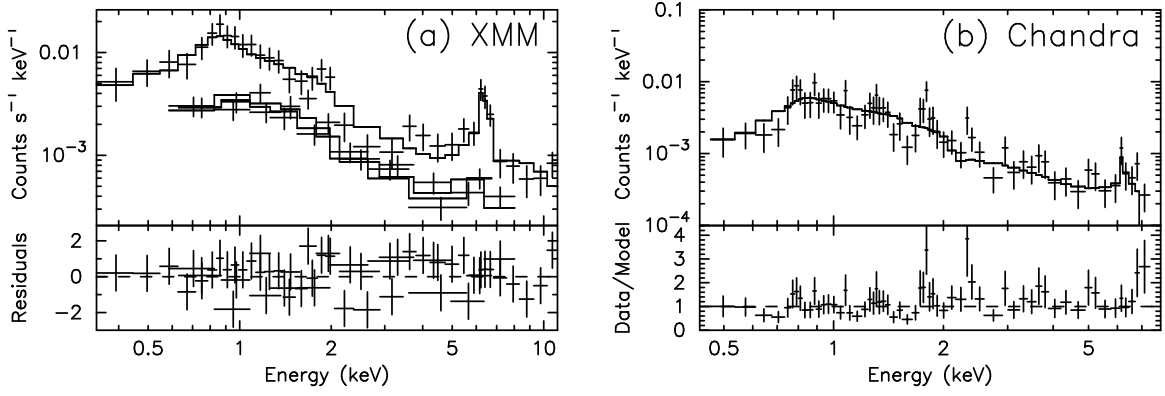


Fig. 2.— (a): An *XMM* EPIC (PN, MOS1, and MOS2) spectrum of UGC 5101, with model A in Table 1 overplotted. In the upper panel, the higher plots are a PN spectrum (which contains the most counts), and the lower plots are MOS spectra. Residuals of the data from the best-fit model are displayed in the lower panel. (b): A *Chandra* ACIS spectrum of the nuclear region. The model A for *XMM* EPIC data is overplotted as a solid line. The lower panel shows the ratio between the data and the model.